

VTT Technical Research Centre of Finland

Multi-sensor optical profilometer for measurement of large freeforms at nm-level uncertainty

Heikkinen, Ville; Nysten, Johan; Byman, Ville; Hemming, Björn; Lassila, Antti

Published in:
Surface Topography: Metrology and Properties

DOI:
[10.1088/2051-672X/abd293](https://doi.org/10.1088/2051-672X/abd293)

Published: 21/12/2020

Document Version
Publisher's final version

License
CC BY

[Link to publication](#)

Please cite the original version:
Heikkinen, V., Nysten, J., Byman, V., Hemming, B., & Lassila, A. (2020). Multi-sensor optical profilometer for measurement of large freeforms at nm-level uncertainty. *Surface Topography: Metrology and Properties*, 8(4), [045030]. <https://doi.org/10.1088/2051-672X/abd293>



VTT
<http://www.vtt.fi>
P.O. box 1000FI-02044 VTT
Finland

By using VTT's Research Information Portal you are bound by the following Terms & Conditions.

I have read and I understand the following statement:

This document is protected by copyright and other intellectual property rights, and duplication or sale of all or part of any of this document is not permitted, except duplication for research use or educational purposes in electronic or print form. You must obtain permission for any other use. Electronic or print copies may not be offered for sale.

PAPER • OPEN ACCESS

Multi-sensor optical profilometer for measurement of large freeforms at nm-level uncertainty

To cite this article: Ville Heikkinen *et al* 2020 *Surf. Topogr.: Metrol. Prop.* **8** 045030

View the [article online](#) for updates and enhancements.



IOP | ebooks™

Bringing together innovative digital publishing with leading authors from the global scientific community.

Start exploring the collection—download the first chapter of every title for free.

Surface Topography: Metrology and Properties



PAPER

Multi-sensor optical profilometer for measurement of large freeforms at nm-level uncertainty

OPEN ACCESS

RECEIVED

21 August 2020

REVISED



25 November 2020

ACCEPTED FOR PUBLICATION

10 December 2020

PUBLISHED

21 December 2020

Ville Heikkinen , Johan Nysten, Ville Byman, Björn Hemming  and Antti Lassila 

VTT Technical Research Centre of Finland Ltd, National Metrology Institute VTT MIKES, Espoo, Finland

E-mail: ville.heikkinen@vtt.fi

Keywords: interferometry, stitching, scanning white light interferometer, confocal, profilometry, metrology

Original content from this work may be used under the terms of the [Creative Commons Attribution 4.0 licence](https://creativecommons.org/licenses/by/4.0/).

Any further distribution of this work must maintain attribution to the author(s) and the title of the work, journal citation and DOI.



Abstract

Optical measurement of large freeform samples is often limited by the resolution, size and slope limits of measurement devices. This trade-off can be solved using stitching—which, however, creates several difficulties often linked to accuracy of movement of the sample or objective. We present a stitching multisensor freeform topography instrument based on scanning white light interferometer, confocal sensor and accurate movements of the sample tracked using laser interferometers. The interferometers track the sample in 2D at an accuracy of a few nm over a 10 cm × 10 cm area. The instrument is thoroughly characterized and uncertainty is estimated to ensure traceable results. Based on the characterization results the instrument allows topography measurement of freeform sample with 54 nm standard uncertainty for datasets of a few hundred sub-images.

1. Introduction

1.1. Metrology for freeform surfaces

Freeform shapes are increasingly used in optics due to their improved functionality and new production methods [1], and may become even more widespread as 3D printing [2] allows creation of customized shapes at relatively low cost. Optical methods would be optimal for their characterization, as scratches from tactile inspection degrade the quality of components. This applies especially to smaller production batches in which all the produced components should be characterized. However, many optical measurement systems designed for conventional spherical optics are not well suited for freeforms.

Devices for measuring 3D profiles fall into three categories: point-to-point measurement devices, line scan sensors and full-field profilometers. Point-to-point systems are flexible, allowing bigger samples to be measured quickly using coarse scans with larger sample-to-sample separation [3–7], but they are generally slow if high-resolution datasets with millions of data points are needed. Line scan systems [8, 9] are fast for many applications, but the sensor width makes them optimal only for a narrow range of sample widths. Thus they are usually very application specific.

Full-field optical profilometers [10, 11] allow fast measurement of a full area of the sample and usually

offer very good vertical precision. However, they are also limited by the magnification used, number of pixels and pixel size. These limit the resolution, imaging area and measurable slope [12–14]. The same instrument typically cannot resolve both small and large features. Normally, an instrument for measuring large areas can only resolve a narrow range of surface slopes [12, 14] due to the numerical aperture (NA), as light gets reflected away from the detector. Additionally for interferometers, if the interference fringe width approaches pixel size or the optical resolution limit of the objective, the measurement signal intensity drops and vertical measurement accuracy is degraded [15, 16]. With higher NA and larger magnification, higher slopes and horizontally smaller features can be measured, but then also the measurement area becomes smaller.

These trade-offs are common for different types of interferometers and there are additional ones for some devices. The trade-off between resolution, imaging area and slope limit may be overcome by image stitching. However, stitching itself has several challenges often linked to accuracy of the movement of the sample/objective.

We describe a novel 2D stitching interferometer based on a scanning white light interferometer (SWLI) and accurately tracked movements of the sample. The

goal is an instrument capable of imaging samples up to 100 cm^2 with precision similar to normal SWLI.

Following things in this paper are novel compared to previous publications: the system described has an order of magnitude larger measurement area combined with high accuracy 2D traceable positioning of the sample; thus the device presented allows accurate stitching of images taken when sample is translated in two directions, and the system relies on characterised flatness of movement for removing tilt within sub-images in both directions. In addition proper characterization of error sources has been done and used for detailed uncertainty budget for the device. Thus the topography of freeform samples up to $10\text{ cm} \times 10\text{ cm}$ can be measured and the measurements are traceable to SI meter.

1.2. Stitching

The measuring area of a full-field profilometer can be extended by stitching several sub-images together [17, 18]. Ideally, this would yield 3D images with similar properties to high magnification images (small horizontal resolution, high measurable slopes), but with a larger field of view (FoV). This would allow using higher magnification for certain samples and also expanding the largest measurable area beyond the limits of the lowest available magnification. There are of course drawbacks to stitching, the most obvious being longer measurement time and high dataset size from combined scans. Another challenge is the stitching algorithm itself; there is always some inaccuracy in combining sub-images, which leads to increased measurement uncertainty.

For stitching in 3D, six degrees of freedom must be matched in areas where sub-images overlap (figure 1 A). This is computationally difficult but can be simplified by eliminating some degrees of freedom experimentally [19, 20].

The approach here is to translate the sample accurately and track the lateral translation and rotation so that only the vertical shift between sub-images needs to be solved (figure 1(B)). The horizontal movement and rotation around the vertical axis is solved by interferometric measurements; tilt is eliminated to the needed precision by the flatness of the sample movement.

1.3. Traceability

All industrial quality assurance measurements should be traceable to SI units, and this applies also for freeform measurements. For traceable results with 3D profilometers such as SWLI, volumetric characterization across three axes is needed. The vertical axis can be calibrated using step height standards and gauge blocks, and horizontal axes using rulers or grids [21]. Out-of-plane error is usually characterized using an optical flat [22]. With stitching, additional errors from sample movement and stitching procedure need to be taken into account.

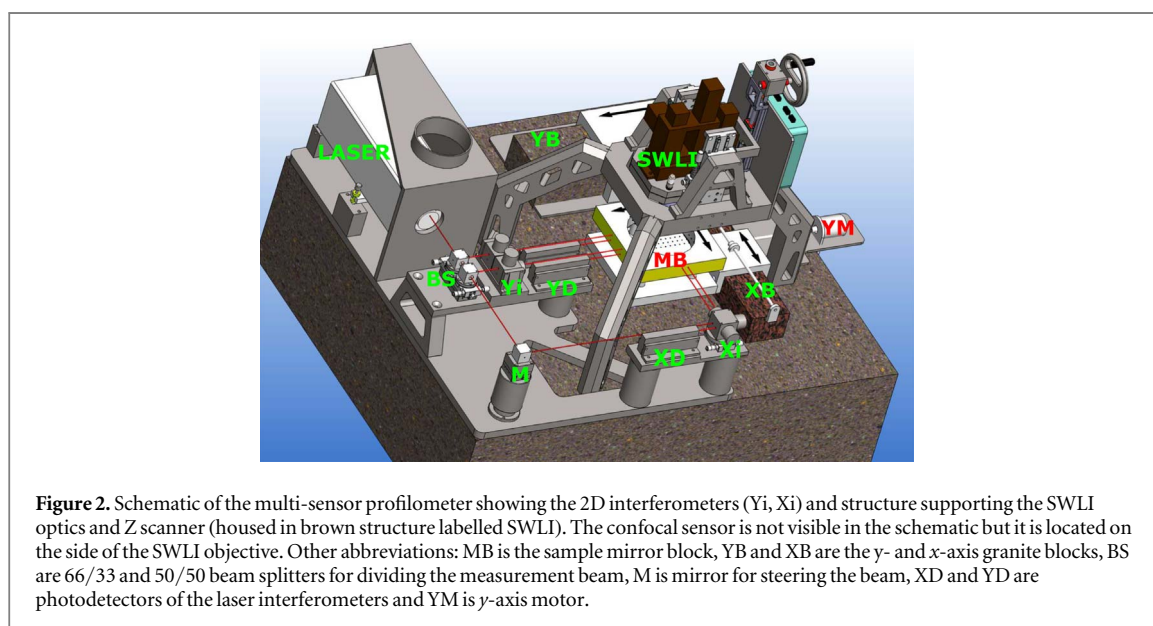
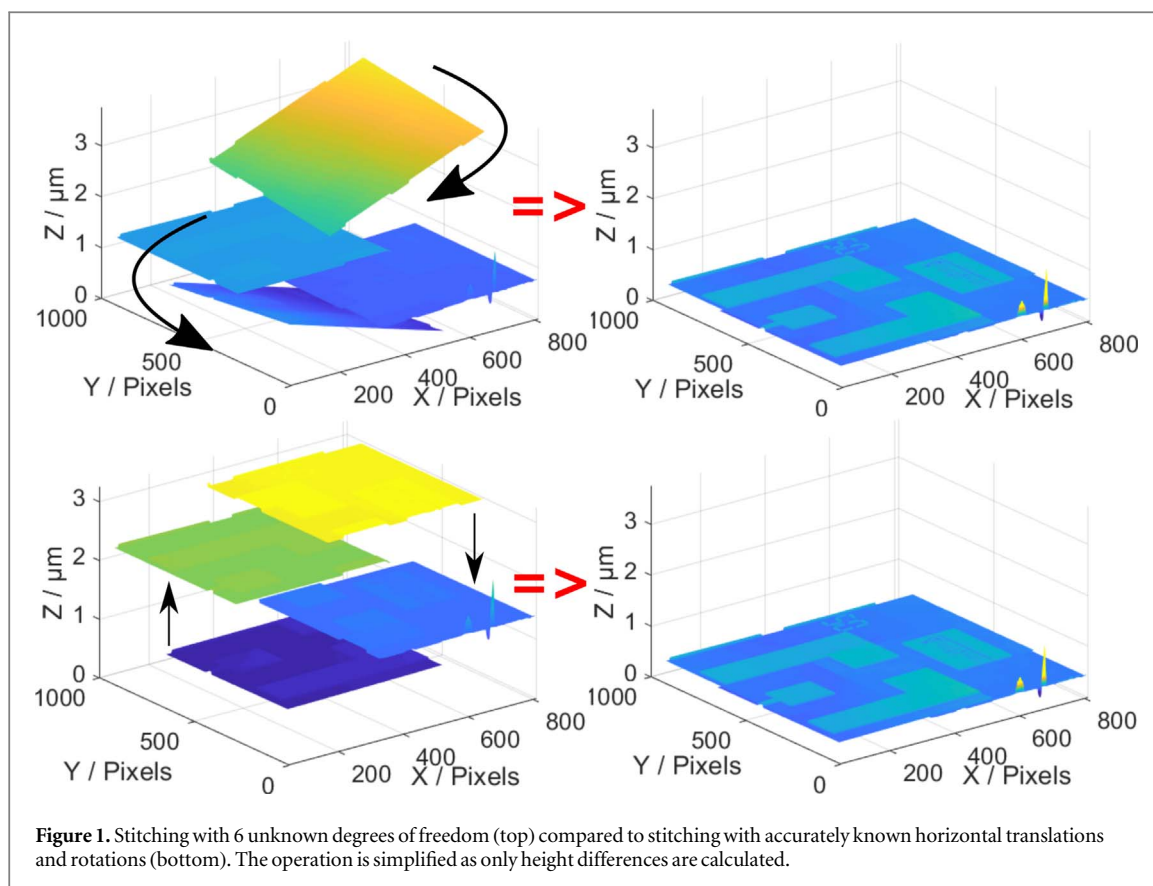
Several components of measurement inaccuracy and motion error are visible in the stitched images. Any error in movement causes errors to the stitching, as the sample is in an incorrect horizontal position or slightly rotated or tilted. Also measurement noise or imaging errors cause uncertainty in stitching. For accurate results, imaging errors should be calibrated out and the horizontal movements between sub-images accurately measured.

2. VTT MIKES multi-sensor optical profilometer

The instrument is based on measurement of sub-images using a scanning white light interferometric microscope head and stitching the images together to a large high-resolution 3D image. The horizontal displacements and rotation of the sample between sub-images are tracked using heterodyne laser interferometers. Straight and accurately tracked movements of the sample allow for correcting only the height difference of sub-images mathematically. There is some deviation from flatness in the granite table, and the zero level of the Z-scale of the SWLI is less accurate than height differences within the measured data; thus the height differences need to be corrected. In the profilometer there is also a chromatic confocal sensor (MICRO-EPSILON IFS 2405-1) for quick coarse scans. In this study we used two different interferometric objectives, both with a $0.55\times$ secondary lens: a $20\times$ Mirau objective with NA of 0.4, which gives a pixel size of $0.881\ \mu\text{m}$ and slope limit of 18.9 degrees on shiny surfaces according to the manufacturer, and a $2.5\times$ Michelson objective with NA of 0.07, which gives a pixel size of $7.10\ \mu\text{m}$ and slope limit of 3 degrees on shiny surfaces according to the manufacturer. The SWLI measures 640×480 pixels in a single scan.

The sample is attached to a holder in the middle of a rectangular mirror block with two 150 mm-long orthogonal mirror faces (see figure 2). The block has a round opening with 125 mm diameter in the middle to allow samples up to that size to be attached on the plane of the laser interferometers to minimize Abbe error. The holder has two axis tilt stages for sample adjustment. The block is supported by three vacuum preloaded air bearings on the granite table and is attached to the x -axis granite block with two vacuum preloaded air bearings. The x -axis granite block runs on the table on two vacuum preloaded air bearings. It is connected to the static y -axis granite block on two horizontal and two vertical vacuum preloaded air bearings. Adjustments of the bearings allow adjustments of orthogonality between the X - and y -axes. Adjusting bearings between the mirror block and the x -axis allows alignment of movement and interferometer axes.

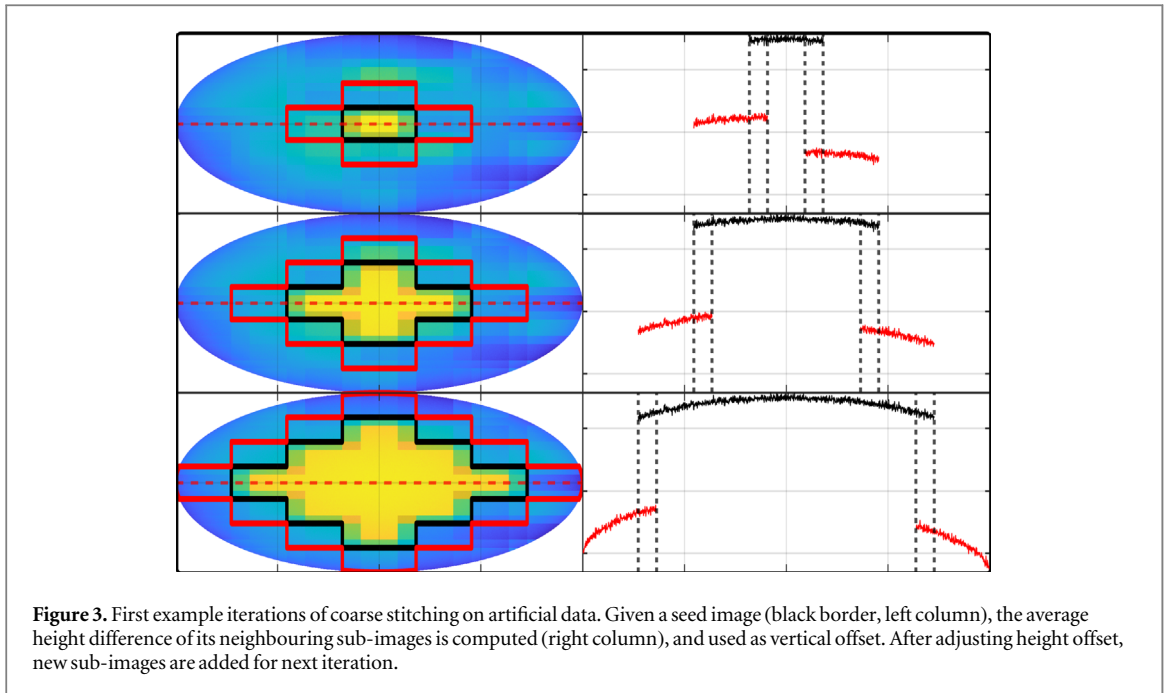
The mirror block position is measured with a laser interferometer along the x -axis and two



interferometers with 40 mm separation along the y-axis. All interferometers are of the double-pass heterodyne type. The optical setup of the interferometers and movement of the mirror block are similar to the 2D interferometer described in [23]. An upgrade to the setup in [23] is that the optical components of the interferometers are placed on invar structures on an invar plate attached to the granite table. Adjustment stages were also added to the beam splitters and beam benders for easier alignment of the beams. The mirror

block structure remains unchanged, with a 2D tilt stage within the block for sample adjustment.

The SWLI and confocal sensors are attached to an invar tripod structure fixed to the granite table (figure 2). The tripod design was chosen to avoid issues due to drifts, bending and vibrations in the long horizontal arms. The trade-offs are restrictions in the placement of oversized samples and added difficulty aligning the two vertical rails used for translating the Z-measurement sensors vertically. Invar was chosen due to its low thermal expansion. The structure



contains an adjustment for tilt of the SWLI sensors and confocal sensor. The height adjustment range is 150 mm in order to fit large samples onto the mirror block if needed. The SWLI sensor head is attached to the setup without modifications, using similar attachment points as in its original support frame. The sensor head includes a camera, illumination and related optics, an objective, a secondary lens and a motor used for z-scans during measurements. The electronics linking the SWLI sensor head to the measurement computer are housed on the support frame and separated from the rest of the setup by a heat shield. The measurement computer and electronics related to the confocal sensor and laser interferometers are enclosed in a ventilated rack to avoid heat load to the measurement setup. The setup is housed at the VTT MIKES measurement laboratory with excellent temperature stabilization, and the stone table is vibration-isolated from the floor [24].

2.1. Stitching algorithm

As the X- and Y-interferometers give the horizontal displacements with sub-pixel accuracy and the measured rotations are sufficiently small, only the height offset between sub-images needs to be adjusted by the stitching algorithm.

The stitching algorithm used here is based on minimizing the residual sum of squares in the overlapping pixels of the sub-images. These goodness metrics were selected to minimize the height difference of all pixels in overlapping image areas.

The stitching algorithm pads sub-images to the full size of the final image, and computes the number of overlapping sub-images for each pixel. The placement of data pixels in each sub-image is determined by measured X-Y sample translations. Then, height

differences of overlapping pixels are corrected by adding a constant vertical offset to the sub-images.

Initial vertical offsets are generated with an iterative coarse stitching algorithm. First, the centremost sub-image is taken as a seed image. Then, in each iteration, the algorithm computes the mean height difference between the seed and all its neighbouring sub-images. The neighbours are then given a vertical offset equal to the mean. Finally, a new seed is generated by adding the height-adjusted neighbours (figure 3). Iteration continues until all sub-images have been added to the seed.

Coarse stitching results in small height differences in areas close to the initial seed sub-image, and larger errors further away from it.

Height differences of sub-images are further reduced using an iterative method based on simulated annealing (simulannealbnd, Matlab 2018b). The vertical offsets obtained in the coarse stitching stage are used as initial values. The objective function in annealing is the residual sum of squares, summed over the overlapping pixels of all sub-images, whose vertical offsets are the function's parameters. Lower and upper bounds on the offsets are set using the function's current value. Iteration continues until the objective function no longer appreciably improves, or to a user-set time limit. For the data used in this work, simulated annealing achieved an order of magnitude improvement in the objective function value from the coarse stitching stage. The final stitched image is composed by first adding the final vertical offsets to the sub-images, and then averaging the pixel values at each location in the image.

Table 1. Uncertainty budget for lateral pixel location, D_x, D_y , using the SWLI for height measurements.

Quantity X_i	Estimate x_i	Uncertainty $u(x_i)$	Probability distribution	Sensitivity coefficient c_i	Uncertainty contribution $u_i(d)$	
					$u(x)$	$u(y)$
Interferometer reading repeatability (m)	0	5 nm	N	1	5 nm	5 nm
Periodic non- linearity (δm_{per})	0	5 nm	arcsine	1	5 nm	5 nm
Wavelength (λ_0)	0	$<10^{-8}$	N	Δx	$<10^{-8} \times \Delta x$	$<10^{-8} \times \Delta y$
Refractive index of air (n)	0	0.14×10^{-6}	N	Δx	$0.14 \times 10^{-6} \times \Delta x$	$0.14 \times 10^{-6} \times \Delta y$
Dead path compensa- tion (δD_{DP})	0	14 nm	R	1	14 nm	14 nm
Mirror block flat- ness (δD_{Mf})	0 nm	22 nm	N	1	22 nm	22 nm
Mirror orthogon- ality ($\delta D_{y, d90}$)	0.87	0.73×10^{-6}	N	Δx	0	$0.02 \times 10^{-6} \times \Delta x$
Abbe error (δD_{Abbe})	0	4.3 nm	N	1	4.3 nm	4.3 nm
Cosine error (δD_{cos})	0	2×10^{-6}	N	Δx	$2 \times 10^{-6} \times \Delta x$	$2 \times 10^{-6} \times \Delta y$
* Pixel size rounding (δD_{pixR})	0	$\frac{1}{2\sqrt{3}}$	R	D_{pix}	$0.29 \times D_{pix}$	$0.29 \times D_{pix}$
* Magnification (D_{pix})	0	10^{-3}	R	x: $320 \times D_{pix}$ y: $240 \times D_{pix}$	$0.32 \times D_{pix}$	$0.24 \times D_{pix}$
* Rotation ($\delta \alpha_m$)	0	2×10^{-4}	R	x: $240 \times D_{pix}$ y: $320 \times D_{pix}$	$0.048 \times D_{pix}$	$0.064 \times D_{pix}$
Sample thermal expan- sion (δD_{xT})	0	0.1×10^{-6}	N	Δx	$0.1 \times 10^{-6} \times \Delta x$	$0.1 \times 10^{-6} \times \Delta y$
Total standard uncer- tainty SWLI $u(D)$	$u(x) = \sqrt{(28 \text{ nm})^2 + (2 \times 10^{-6} \times \Delta x)^2 + 0.43 \times D_{pix}}$ $u(y) = \sqrt{(28 \text{ nm})^2 + (2 \times 10^{-6} \times \Delta y)^2 + (0.02 \times 10^{-6} \times \Delta x)^2 + (0.38 \times D_{pix})^2}$					

Table 2. Uncertainty budget confocal XY-axis. First two terms contain terms from table 1 apart from those marked*.

Quantity X_i	Estimate x_i	Uncertainty $u(x_i)$	Probability distribution	Sensitivity coeffi- cient c_i	Uncertainty contribution $u_i(d)$
Constant terms similar to SWLI	0	19 nm	N	1	19 nm
Linear terms similar to SWLI	0	2×10^{-6}	N	Δx	$2 \times 10^{-6} \times \Delta x$
Spot size (δD_{spot})	0	2000 nm	N	1	2000 nm
Total standard uncertainty confocal $u(D)$	$\sqrt{(2000 \text{ nm})^2 + (2 \times 10^{-6} \times \Delta x)^2}$				

2.2. Characterization of the instrument and uncertainty budget

To ensure the traceability of measurements, the instrument was thoroughly characterized and the uncertainty budget calculated based on the characterization.

2.2.1. Lateral scale

In the following, we analyse the uncertainty components of the final stitched-image camera pixel locations and give the combined uncertainty for the SWLI (table 1) and for the confocal sensor (table 2).

The model for lateral measurement is the following for the camera pixel, $D_{xCenter}$ in the centre of the image:

$$D_{xCenter} = \frac{(m + \delta m_{per})\lambda_0}{2n(p, t_{air}, h)} + \delta D_{DP} + \delta D_{Mf} + \delta D_{y, d90} + \delta D_{Abbe} + \delta D_{cos},$$

where m is the interferometer counter reading; δm_{per} is the interferometer nonlinearity correction; λ_0 is the vacuum wavelength of the laser; n is the refractive index of air, which depends on air pressure p , temperature t_{air} and humidity h ; δD_{DP} is the correction due to refractive index changes within the interferometer dead path; δD_{Mf} is the correction for mirror block flatness; $\delta D_{y, d90}$ is the correction for non-orthogonality of the X- and y-axes; δD_{Abbe} is the correction for abbe error; and δD_{cos} is the correction for cosine error due to laser alignment. The same formula applies to the horizontal position of the confocal sensor.

The model for the single-image pixel location along the x -axis is:

$D_{xPix} = n_{pixX} \times D_{pix} + n_{pixY} \times \alpha_m \times D_{pix}$, where D_{pix} is the pixel size after magnification, n_{pixX} and n_{pixY} are the number of pixels along x and y , and α_m is the rotation of the mirror block. The function for the y -axis is similar.

Next, the model for the stitched-image pixel location, D_x , is combined from the formulae for central pixel position, pixel position within a sub-image, and additional terms for correction of the thermal expansion of the sample δD_{xT} to 20 °C and correction due to pixel size rounding δD_{pixR} :

$$D_x = D_{xCenter} + \delta D_{xPix} + \delta D_{pixR} + \delta D_{xT}.$$

In the following, the uncertainties of different input parameters are estimated. The combined uncertainty is presented in table 1 for the SWLI and table 2 for the confocal sensor. The standard uncertainty of the interferometer reading due to repeatability of interferometers and noise of air bearings, m , was determined to be 5 nm based on the noise level of the results. The laser interferometer has periodic non-linearity, δm_{per} , which is estimated to have a standard uncertainty contribution of 5 nm. In this work, this was seen as negligible and the nonlinearity was not reduced further.

The frequency of the HeNe laser used in the XY interferometer has been calibrated to within $<1 \times 10^{-8}$, thus the effect of the vacuum wavelength λ_0 on the measurement uncertainty is negligible.

The refractive index of air, n , is a function of air pressure, temperature and humidity. The laboratory has thermal and humidity control and the pressure is measured. Only changes in n due to pressure are compensated for in the results. The typical range of air temperature, t_{air} , (less than 0.1°C) and humidity ($\pm 3.3\%$) cause a 1×10^{-7} uncertainty contribution. The uncertainty of the pressure, p , measurement is 20 Pa, which causes an uncertainty contribution of 1×10^{-7} . The total uncertainty contribution from the refractive index of air determination is thus 1.4×10^{-7} .

The dead path length is 100 mm and is known to within ~ 1 mm. With the typical pressure change during measurement, the uncertainty contribution due to dead path correction δD_{DP} is estimated to be 14 nm.

Flatness deviations of the mirror block surfaces, D_{Mf} , are measured to be 48 nm for the X-face and 41 nm for the Y-face, peak to valley. The standard uncertainty of these measurements is 18 nm. The uncertainty contribution of the uncorrected flatness of the mirrors D_{Mf} is estimated to be 22 nm [23].

In an earlier test, the orthogonality deviation of the mirror block was measured to be 0.87 μ rad using an autocollimator and a rotary table [23]. The uncertainty contribution of the orthogonality correction, $\delta D_{y, a90}$, is $0.73 \times 10^{-6} \times \Delta x$ to the Y-values.

Abbe error is caused by sample tilt and the difference of the measurement position from the

interferometer plane. The standard uncertainty of the sample tilt is estimated to be 1.42×10^{-6} . For typical measurements, the sample surface is within 3 mm of the interferometer plane. Thus, the uncertainty of the Abbe error correction, δD_{Abbe} , for both X and Y is 4.3 nm.

Cosine error is due to non-aligned laser beams. The beams were calculated to deviate by maximum 0.0020 rad from the normal of the mirrors, which defines the measurement axes. This causes an uncertainty contribution of 2×10^{-6} for uncompensated cosine error δD_{cos} .

For both the confocal sensor and SWLI, the dominating source of lateral measurement uncertainty is the lateral resolution the sensor. For the SWLI, the pixel sizes with the magnifications used in this work were 0.9 μ m and 7.2 μ m. The uncertainty contribution of rounding the results to the pixel size, δD_{pixR} , is estimated to be 0.26 μ m and 2.1 μ m, respectively.

The rotation of the mirror block around vertical axis was measured to be 2×10^{-4} rad when moving along the y -axis and 8×10^{-5} along the x -axis (figure 4). This rotation is unimportant for confocal measurements. For SWLI measurements, the uncompensated rotation α_m causes an uncertainty contribution of 0.048 pixels for x and 0.064 pixels for y position values (at the image edges).

Thermal expansion of the sample causes only a minor error thanks to good thermal control of the measurement room and small sample size. The estimated uncertainty contribution due to the uncompensated thermal expansion correction, δD_{xT} , is estimated to be $0.1 \times 10^{-6} \times \Delta x$ for a steel sample.

The uncertainty contributions of all other sources combined are much less than the uncertainty of the correction due to pixel size rounding, δD_{pixR} , with a magnitude of $\frac{1}{2\sqrt{3}} \times D_{pix}$. The same applies to the confocal sensor, with an uncertainty of measurement position within spot size δD_{spot} causing 2000 nm uncertainty in the horizontal position.

In the tests, the sample movement along the y -axis was straight to within 2.7 μ m, and along the x -axis to within 0.16 μ m. Crosstalk due to angle errors of movement and measurement axes was 3.7×10^{-5} μ m from Y to X and 2.0×10^{-5} μ m from X to Y. These cause offsets in the measurement positions, but the offsets are tracked accurately using the laser interferometers and thus do not cause errors to the combined 3D profile. However, they need to be taken into account when planning the measurements if exact positions are required.

2.2.2. Vertical scale

The model for measured pixel height, H , with the SWLI is:

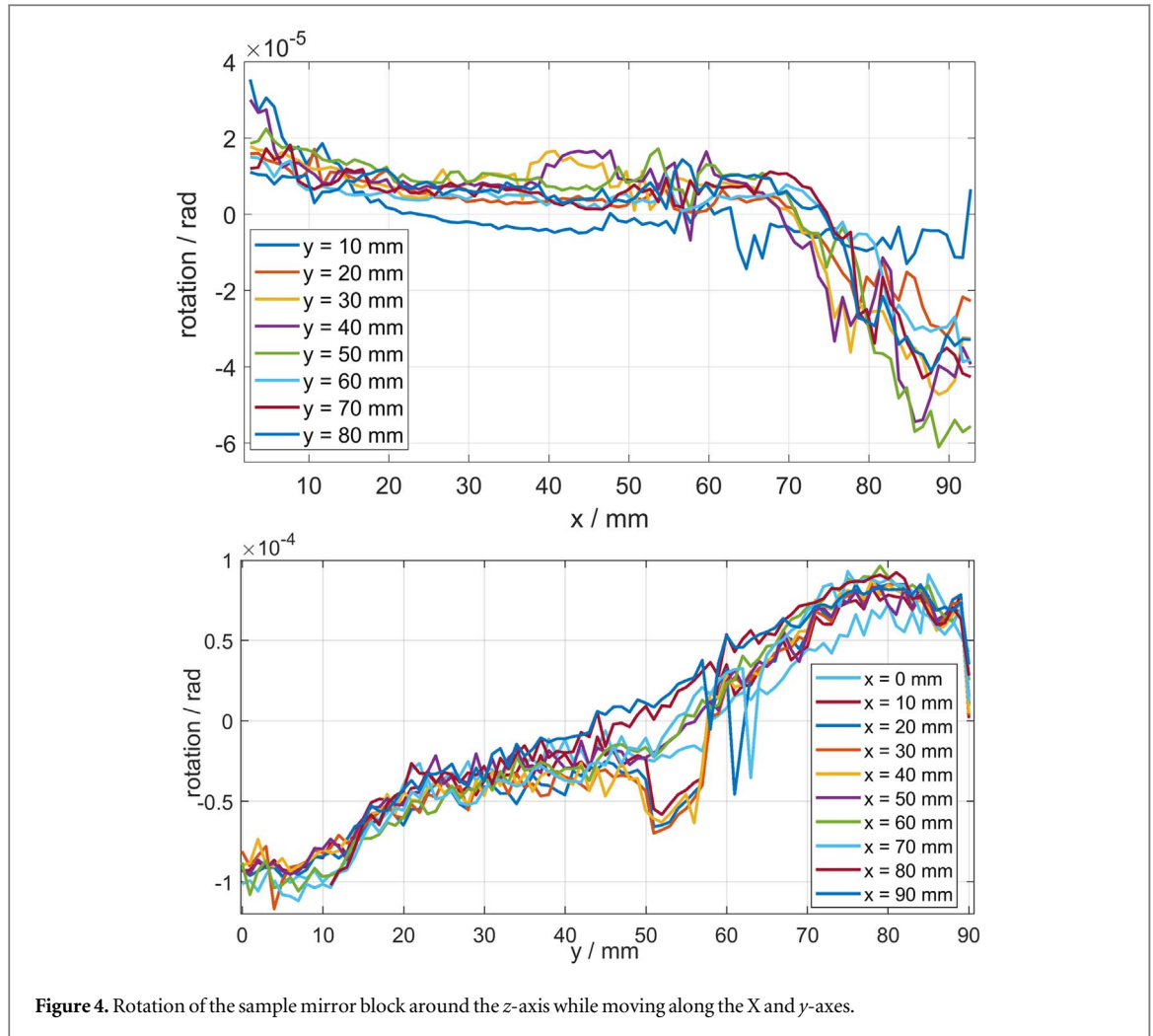


Figure 4. Rotation of the sample mirror block around the z-axis while moving along the X and y-axes.

$$H = (\delta g + \delta g_{nonl} + \delta g_{per})h + \delta h_{oop} + \delta h_{st} + \delta h_{tilt} + \delta h_{noise}$$

where δg is the gain correction of the SWLI linear position encoder, δg_{nonl} is the nonlinearity correction of the encoder over long distances, δg_{per} is the periodic nonlinearity correction of the sensor at $\leq 10 \mu\text{m}$ scale, h is the encoder height reading, δh_{oop} is the out-of-plane correction of the SWLI within one image, δh_{st} is the stitching correction, δh_{tilt} is the correction for tilt of the sub-images, and δh_{noise} is the pixel noise of the image.

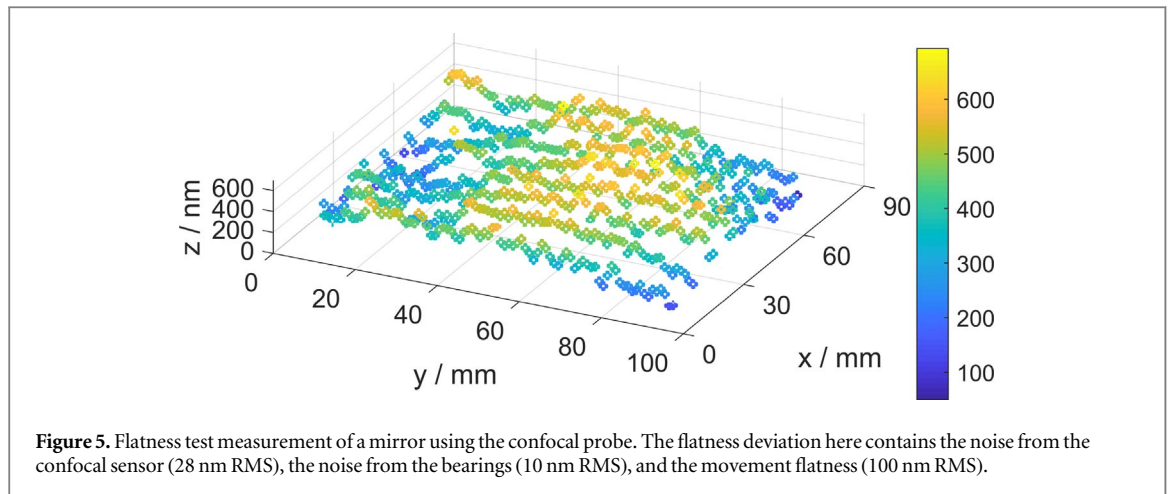
The Z-scale of the SWLI was calibrated using gauge blocks up to 1 mm and step height standards down to sub- μm scale. These transfer standards were measured at various positions along the used part of the z-axis. Based on these measurements, the uncertainty of the gain correction, δg , was determined to be $10.6 \times 10^{-6} \times \Delta h$ and the uncertainty of the large scale nonlinearity correction, δg_{nonl} , of the scale $144 \times 10^{-6} \times \Delta h$. The gauge blocks were calibrated using a phase stepping gauge block interferometer [25] and the lowest step height standards using an AFM [26].

In addition to the step height standards, the small-scale nonlinearity was characterized by measuring a

tilted mirror to see it in finer detail and across several periods. The Z-scanner has periodic nonlinearity with period of $10.4 \mu\text{m}$ and peak-to-peak amplitude of 25 nm. Additionally, with a period of 270 nm (1/2 of the mean light wavelength), there is a nonlinearity of 7 nm peak to peak. The combined uncertainty contribution of these uncompensated periodic nonlinearity error components δg_{per} is 9 nm.

The out-of-plane error correction of the SWLI (δh_{oop}) was defined by measuring a flat sample at several different positions (to further decrease the effect of the sample) and fitting a low order polynomial surface to the average measured profile. The uncertainty of the out-of-plane correction is 1 nm. For optimal results, correction of the out-of-plane error always needs to be done after adjusting the objective or the secondary lens.

Uncertainty due to the stitching error ($\delta h_{st}Z$) is 10 nm in a stitched seam between two positions in a typical sample with $\sim 20\%$ image overlap at the seams. Stitching errors are assumed to be random; thus over many seams the error only grows as a function of the square root of the number of seams between two points. This was estimated based on the height differences between the sub-images at the seams of the combined profiles with different shapes. For flat profiles, a



slightly better stitching accuracy can be reached than for highly curved shapes. Typically, small profiles have slightly smaller stitching errors than large combined profiles with several sub-images.

Movement flatness of the sample holder was defined from the measurement of a flat mirror (figure 3). The movement flatness is corrected by stitching, and only the tilting of the sample holder affects the SWLI measurements causing error. Tilt also decreases stitching accuracy, but that contribution is included in the stitching term δh_{st} . The magnitude of tilt was defined based on the recorded height differences within the measurement area divided by the distance of the air bearings. The tilt of the sample (1.4×10^{-6} rad) during translations causes an uncertainty contribution for the SWLI relative to the measurement area of a sub-scan. For the lowest magnification, the uncertainty contribution of uncompensated tilt, δh_{tilt} , is 3.2 nm, less at higher magnifications.

The noise due to air bearings also decreases the vertical precision of the SWLI. When measuring on air bearings, the noise and repeatability of the SWLI measurements δh_{noise} cause a measurement uncertainty of 5 nm. Without the noise from the air bearings, the noise level of the SWLI would be <1 nm for flat samples measured in this work.

The model for height measurement with confocal sensor is:

$$H = (\delta g + \delta g_{nonl})h + \delta h_{flat} + \delta h_{noise},$$

where δg is the gain correction of the confocal sensor, δg_{nonl} is the nonlinearity correction of the sensor, h is the measured height (the former terms depend on height), δh_{flat} is the flatness of the sample movement, and δh_{noise} is the noise of the confocal sensor and air bearings.

The gain correction of the confocal sensor δg is estimated to have an uncertainty of $100 \times 10^{-6} \times \Delta h$.

The linearity error of the confocal sensor at large scale, δg_{nonl} , was defined to be 100 nm. This is in line with manufacturer specifications and the results

published by others for other chromatic confocal sensors [27, 28].

To characterize flatness and vertical noise of the rebuilt 2D translation and the interferometers, we measured a $10 \text{ cm} \times 10 \text{ cm}$ area of a flat mirror (calibrated deviation from flatness <50 nm) using the chromatic confocal probe (figure 5). This allowed us to see the movement straightness of the sample as it moved along the X and Y axes, and as well as its vertical movement and vibration (figure 5).

The measured deviation from flat was 110 nm RMS. The noise level of the confocal sensor and air bearings was 30 nm. Assuming these are non-correlated, there is a 100 nm RMS deviation from flatness δh_{flat} .

The noise level of the bearings and confocal probe was defined from tests with a static mirror and air pressure on and off. In static tests, the noise of the confocal sensor was 30 nm RMS with air on and 28 nm RMS with air off. From these results, the vibration level was defined to be 10 nm RMS based on a 2 nm rise to the confocal sensor level (28 nm). In the uncertainty budget, the 30 nm repeatability value of δh_{noise} contains the contributions of the bearings and the confocal sensor.

Uncertainty due to thermal expansion of the sample is negligible ($<10^{-6}$) for all typical materials, as the laboratory temperature is well controlled and other error sources limit the accuracy to a level of 10^{-4} .

2.2.3. Combined uncertainty

The combined uncertainties in tables 1–4 correspond to the X, Y or Z separation of two measured pixels within the measured profile with n_{seams} number of seams between sub-images, height separation Δh , and horizontal separation Δx , Δy apart from each other.

For the X- and y-axes, the movements are precise enough that the uncertainty contribution of pixel size rounding δD_{pixR} and uncertainty of pixel size D_{pix} is bigger than the other sources combined. For the confocal sensor, the same applies to the spot size (δD_{spot}),

Table 3. Uncertainty budget for stitched SWLI z-axis.

Quantity X_i	Estimate x_i	Uncertainty $u(x_i)$	Probability distribution	Sensitivity coeffi- cient c_i	Uncertainty contribution $u_i(d)$
Periodic nonlinearity of encoder and surface detection (δg_{per})	0	10 nm	arcsine	1	9 nm
Repeatability (δh_{noise})	0	5 nm	N	1	5 nm
Scale nonlinearity (δg_{nonl})	0	144×10^{-6}	R	Δh	$144 \times 10^{-6} \times \Delta h$
Amplification error (δg)	0	10.6×10^{-6}	N	Δh	$10.6 \times 10^{-6} \times \Delta h$
Sample thermal expansion (δD_{xT})	0	0.1×10^{-6}	N	Δh	$0.1 \times 10^{-6} \times \Delta h$
Stitching error (δh_{st})	0	10 nm	N	$\sqrt{n_{seams}}$	$10 \text{ nm} \times \sqrt{n_{seams}}$
Out-of-plane error (δh_{oop})	0	1 nm	R	1	1 nm
Tilt of sub-images (δh_{tilt})		1.42 nm/mm	N	$320 \times D_{pix}$	$\leq 3.2 \text{ nm}$
Total standard uncertainty $u(H)$					$\sqrt{(10.8 \text{ nm})^2 + (144 \times 10^{-6} \times \Delta h)^2 + (10 \text{ nm} \times \sqrt{n_{seams}})^2}$

Table 4. Uncertainty budget confocal z-axis.

Quantity X_i	Estimate x_i	Uncertainty $u(x_i)$	Probability distribution	Sensitivity coeffi- cient c_i	Uncertainty contribution $u_i(d)$
Movement flatness (δh_{flat})	0	100 nm	N	1	100 nm
Repeatability (δh_{noise})	0	30 nm	N	1	30 nm
Scale nonlinearity (δg_{nonl})	0	50 nm	R	1	50 nm
Amplification error (δg)	0	100×10^{-6}	N	Δh	$100 \times 10^{-6} \times \Delta h$
Sample thermal expansion (δD_{xT})	0	0.1×10^{-6}	N	Δh	$0.1 \times 10^{-6} \times \Delta h$
Total standard uncertainty $u(H)$					$\sqrt{(116 \text{ nm})^2 + (100 \times 10^{-6} \times \Delta h)^2}$

which is a bigger uncertainty source (500 nm) than those related to positioning.

For the SWLI z-axis measurements, the main components are periodic nonlinearity of the height scale, δg_{per} , stitching errors, δh_{st} and repeatability (δh_{noise}). For larger heights, also the large-scale nonlinearity of the SWLI Z-scale δg_{nonl} becomes important (see table 3).

For the confocal sensor, the movement flatness δh_{flat} is the most important source of height measurement uncertainty (see table 4).

3. Results

3.1. Stitching test

To test the system, we measured samples with steep slopes using a $20\times$ objective and $0.55\times$ secondary lens, and larger areas of flatter samples using a $2.5\times$ objective and $0.55\times$ secondary lens.

In the test of the flatter samples, a stitching accuracy of ~ 10 nm was achieved for low magnification sub-images (figure 6). The sample is made of zerodur with nominal $7 \mu\text{m}$ scale height differences and small marker feature in the middle [29]. It is clear in the stitched dataset that some of the residual error is due to tilting of the sample during motion, as there is often an almost perfectly aligned area in the middle of the seam.

In high magnification test (figure 7), objective areas with slopes of up to 15° were measured and 250 sub-images were combined into one dataset (figure 7) spanning 1 mm vertically and $18 \text{ mm} \times 8 \text{ mm}$ laterally. The convex sample is made of invar and features different 2 radii of curvature 39.5 mm and 40 mm.

4. Discussion

Samples up to 50 mm in diameter and 1 mm in height were measured using the built interferometer. The standard uncertainty of measurement of the stitched data could be kept close to that of a typical SWLI. For the larger diameter sample in figure 6, the uncertainty of the stitched SWLI data was 54 nm, whereas that of a SWLI measurement of similar height in a sample that fits into a single scan would be 38 nm. For the taller sample in figure 7, the measurement uncertainty of 124 nm is even closer to that of a single scan measurement of similar height (115 nm). Results of a recent comparison support that the measurement results are within the stated uncertainty [29]. With a chromatic confocal sensor, the measurement uncertainty is only slightly worse (119 nm and 141 nm). Thus, it is not only useful for alignment of samples but also for quick measurements in cases where coarser horizontal resolution is sufficient. The chromatic

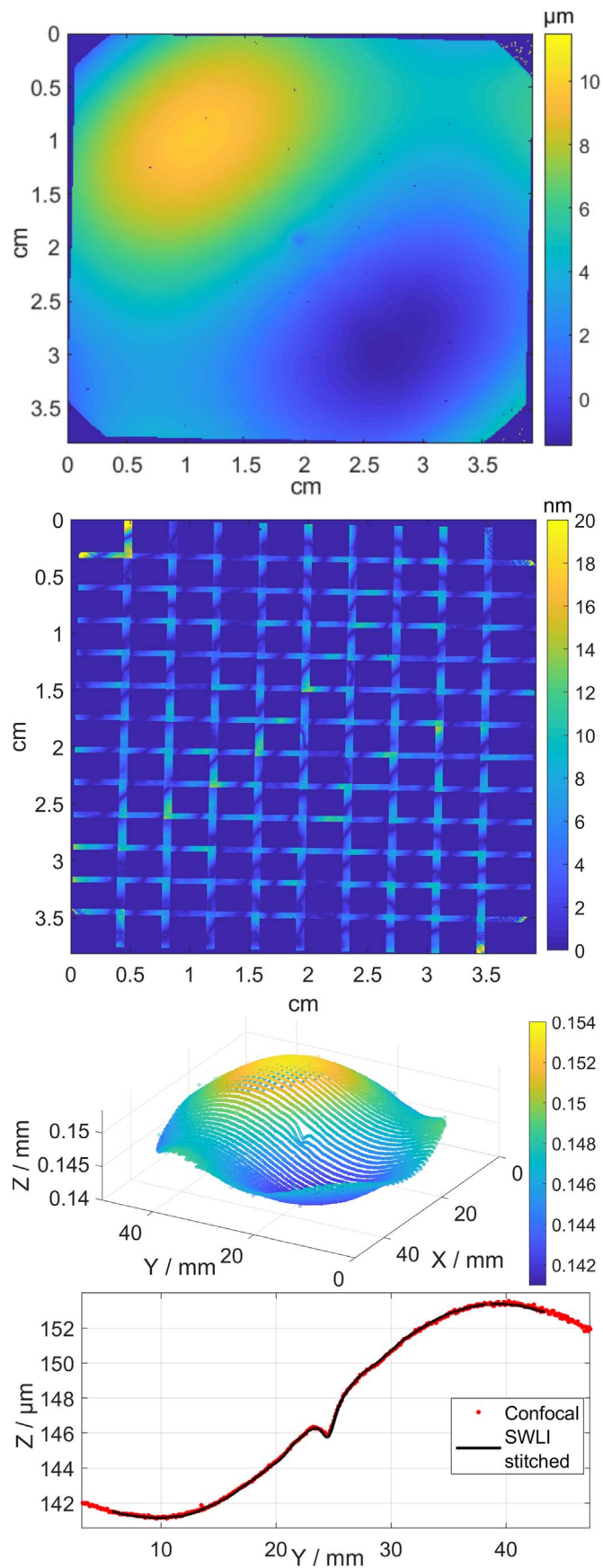
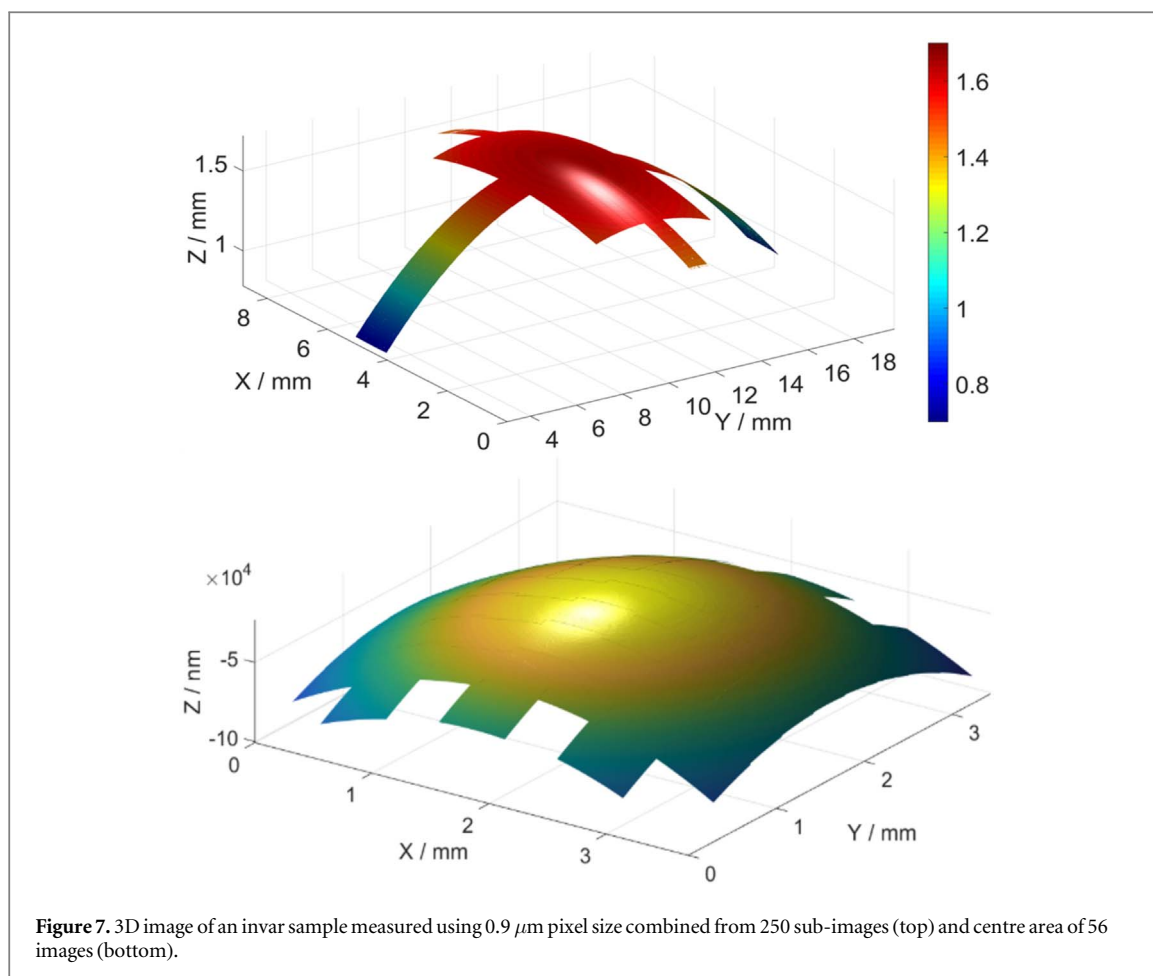


Figure 6. Height map created by stitching 130 sub-images together (top), and standard deviation of overlapping pixels (second) illustrating stitching accuracy. The same sample measured using the confocal sensor (third) and results of the two at centreline of the sample (bottom).



confocal sensor in the setup was found to have good ability to measure steep slopes with the signal visible from slopes up to 30° described in the specifications. However, at high slopes the linearity of confocal sensors may be degraded [5, 27, 28].

5. Conclusions

A novel multi-sensor profilometer was built for measuring cm-sized freeform samples. The methodology for stitching was developed and described. The profilometer was tested by measuring samples with sizes of up to $5\ \text{cm} \times 5\ \text{cm}$, with the largest datasets consisting of 300 sub-images for the SWLI and 35,000 data points for the confocal sensor. The uncertainty budget is presented, and the test results show good agreement with the calculated uncertainty budget.

The instrument could be further improved by thorough SWLI calibration at small scales across the full vertical measurement range, compensating for the effect of $10\ \mu\text{m}$ – $1000\ \mu\text{m}$ scale nonlinearities in the analysis software. Additionally, a feedback system could be built to allow exact placement of pixels during horizontal shifts. With these improvements, also improving temperature stability and reducing vibrations within the air bearings would be useful. Currently, the thermal stability is sufficient and the

vibration levels are acceptable, as the horizontal precision is limited to pixel scale and vertical precision to tens of nanometres due to scale nonlinearity. Full automation of measurements would make measurements of 500+ sub-images more feasible.

Measurement uncertainty of stitched data could be kept close to that of a typical SWLI, while the horizontal range could be improved by a factor of 20. The chromatic confocal sensor in the setup was found to have relatively good height sensitivity and ability to measure steep slopes.

In conclusion, the developed system based on stitching aided by laser interferometers can measure large ($50\ \text{mm}$ diameter, $260\ \mu\text{m}$ high) freeform samples at $54\ \text{nm}$ standard uncertainty.

Acknowledgments

This work is part of project 15SIB01 FreeFORM which has received funding from the EMPIR programme co-financed by the Participating States and from the European Union's Horizon 2020 research and innovation programme.

ORCID iDs

Ville Heikkinen  <https://orcid.org/0000-0002-9208-5501>

Björn Hemming  <https://orcid.org/0000-0001-8519-0656>

Antti Lassila  <https://orcid.org/0000-0002-6991-7082>

References

- [1] Kotz F, Arnold K, Bauer W, Schild D, Keller N, Sachsenheimer K, Nargang T M, Richter C, Helmer D and Rapp B E 2017 *Nature* **544** 337–9
- [2] Assefa B G, Saastamoinen T, Biskop J, Kuittinen M, Turunen J and Saarinen J 2018 *J. Opt. Rev.* **25** 456–62
- [3] Noura H et al 2014 *Meas. Sci. Technol.* **25** 044016
- [4] Buajarern J, Kang C-S and Kim J W 2014 *Surface Topography: Metrology and Properties* **2** 014003
- [5] Boltryk P J, Hill M, McBride J W and Nasce A 2008 *Sens. Actuators A: Phys.* **142** 2–11
- [6] Křen P 2008 *Meas. Sci. Technol.* **19** 107001
- [7] Schulz M, Geckeler R and Illemann J 2003 *Proc. SPIE* **5190** 211–220 <https://doi.org/10.1117/12.503700>
- [8] Seppä J, Niemelä K and Lassila A 2018 *Measurement Science and Technology* **29** 5
- [9] Im K-V, Han S, Park H, Kim D and Kim B-M 2005 *Optics Express* **13** 5151–6
- [10] Harasaki A, Schmit J and Wyant J C 2000 *Applied Optics* **39** 13 <https://doi.org/10.1364/AO.39.002107>
- [11] Schmit J, Reed J, Novak E and Gimzewski J K 2008 *Opt. A: Pure Appl. Opt.* **10** 064001
- [12] Xie W, Lehmann P and Niehues J 2012 *Applied Optics* **51** 11
- [13] Savio E, De Chiffre L and Schmitt R 2007 Metrology of freeform shaped parts *Annals of the CIRP* **56** 2
- [14] Giusca C, Leach R, Helery F and Gutauskas T 2011 *Journal of Physics: Conference Series* **311** 012005
- [15] Lehmann P, Tereschenko S and Xie W 2016 *Surface Topography: Metrology and Properties* **4** 024004
- [16] Liu M, Cheung C F, Ren M and Cheng C-H 2015 *Applied Optics* **54** 8670
- [17] Yumoto H, Mimura H, Handa H, Kimura T, Matsuyama S, Sano Y, Ohashi H, Yamauchi K and Ishikawa T 2010 *Nuclear Instruments and Methods in Physics Research A* **616** 203–6
- [18] Leia Z, Liua X, Zhaob L, Chena L, Lia Q, Yuana T and Lu W 2016 *Optics Communications* **359** 435–47
- [19] Kapusi D, Machleidt T, Manske E, Franke K-H and Jahn R 2008 *Proc. 12th Int. Coll. on Surfaces* 210–7
- [20] Xue J, Huang L, Gao B, Kaznatcheev K and Idir M 2017 *Optics Express* **25** 9393–405
- [21] Giusca C, Leach R and Helery F 2012 *Meas. Sci. Technol.* **23** 065005
- [22] Giusca C, Leach R, Helery F and Gutauskas T T 2011 *J. Phys.: Conf. Ser.* **311** 012005
- [23] Hemming B, Palosuo I and Lassila A 2002 *Proc of SPIE* **4902** 670–8
- [24] Lassila A et al 2011 *Measurement* **44** 399–425
- [25] Byman V and Lassila A 2015 *Measurement Science and Technology* **26** 084009
- [26] Korpelainen V, Seppä J and Lassila A 2010 *Precision Engineering* **34** 735–44
- [27] Noura H, El-Hayek N, Yuan X and Anwer N 2014 *Meas. Sci. Technol.* **25** 044011
- [28] Noura H, El-Hayek N, Yuan X, Anwer N and Salgado J 2014 *J. Phys.: Conf. Ser.* **483** 012015
- [29] o Arezki Y 2019 Robust reference algorithms for form metrology: Application to aspherical and freeform optics *Doctoral Thesis ENS Paris-Saclay* p 97–123 <http://www.theses.fr/en/2019SACLN058>